Icarus 389 (2023) 115232

Contents lists available at ScienceDirect

Icarus

journal homepage: www.elsevier.com/locate/icarus

Research Paper

The influence of heterogeneous seafloor heat flux on the cooling patterns of Ganymede's and Titan's subsurface oceans

Filipe Terra-Nova [a,b,*], Hagay Amit [b], Gaël Choblet [b], Gabriel Tobie [b], Mathieu Bouffard [c], Ondřej Čadek [d]

[a] Departamento de Geofísica, Instituto de Astronomia, Geofísica e Ciências Atmosféricas, Universidade de São Paulo, Rua do Matão, 1226, Cidade Universitária, 05508-090, São Paulo, Brazil
[b] Laboratoire de Planétologie et Géosciences, CNRS UMR 6112, Nantes Université, Université d'Angers, Le Mans Université, Nantes, France, 2 rue de la Houssinière, F-44000 Nantes, France
[c] Aix Marseille University, CNRS, Centrale Marseille, IRPHE, Marseille, France
[d] Charles University, Faculty of Mathematics and Physics, Department of Geophysics, V Holešovičkách 2, Prague 18000, Czech Republic

ARTICLE INFO

Dataset link: https://magic-sph.github.io/

Keywords:
Icy moons
Titan
Ganymede
Hydrodynamics
Heat transfer

ABSTRACT

Several icy moons of Jupiter and Saturn are known to possess deep water oceans. Heating in the rocky mantle underneath often produces heterogeneous heat flux patterns at the ocean's seafloor. How this internal ocean dynamically relates the seafloor to the surface ice shell is a crucial question to understand the long term evolution of icy moons. Here we investigate how a heterogeneous seafloor heat flux pattern affects the convection and heat transfer in the subsurface ocean of large icy worlds involving a high pressure ice layer beneath the seafloor such as Titan or Ganymede. We perform rotating convection simulations in a thin 3D spherical shell with a prescribed heterogeneous bottom heat flux inferred from 3D convection simulations of the underlying mantle (Choblet et al., 2017b). In our simulations, although the amplitude of imposed inner boundary heat flux heterogeneity is rather moderate, preferred longitudes of intense outer boundary heat flux are highly correlated with longitudes of intense inner boundary heat flux. In addition, a small imposed inner boundary large-scale order 2 pattern is amplified at the outer boundary heat flux by the convection in the thin shell. Lastly, deviations from axisymmetry and equatorial symmetry in the outer boundary heat flux increase with the main convection vigor and the amplitude of the inner boundary heterogeneity. In our models polar vs. equatorial cooling is mostly controlled by inertial effects, as was found by Amit et al. (2020) for homogeneous boundary conditions, with the latitudinally equilibrated inner boundary heterogeneity acting to reduce the amplitude of this effect. Our results support polar cooling for Titan's sub-surface ocean.

1. Introduction

The exploration of Jupiter's and Saturn's systems, by the Galileo and Cassini–Huygens missions respectively, has revealed that several moons harbor salty water oceans underneath their icy crusts (see Hussmann et al., 2015, for a review). Earlier predictions based on thermal evolution models (e.g. Kirk and Stevenson, 1987; Grasset and Sotin, 1996; Tobie et al., 2005) have thus been confirmed by various geophysical detection techniques. Magnetic induction caused by the moons' orbits in a tilted Jovian magnetosphere enabled the identification of global scale conductive layers in Europa, Ganymede and Callisto (Khurana et al., 1998, 2002; Zimmer et al., 2000; Kivelson et al., 2002). Owing to the presence of an internal dynamo, the more ambiguous measurement in the case of Ganymede was later confirmed by Earth-based observation of auroral oscillations (Saur et al., 2015). In the system of Saturn, low frequency electric waves observed in Titan's atmosphere by the Huygens probe first hinted at a deep conducting interface beneath the ice (e.g. Béghin et al., 2012) although this interpretation has been recently challenged (Lorenz and Le Gall, 2020). The presence of an ocean was indicated by the observation of an abnormally high obliquity (Baland et al., 2011) and further confirmed by the detection of internal gravitational tides (Iess et al., 2012), indicating the existence of a liquid layer at depth decoupling the outer shell from the deep solid interior.

No direct observations are available to constrain the dynamics of internal oceans, however long-wavelength topography and gravity data can be used indirectly to shed light on heat transfer conveyed by

* Corresponding author at: Departamento de Geofísica, Instituto de Astronomia, Geofísica e Ciências Atmosféricas, Universidade de São Paulo, Rua do Matão, 1226, Cidade Universitária, 05508-090, São Paulo, Brazil.
E-mail address: filipeterranova@gmail.com (F. Terra-Nova).

https://doi.org/10.1016/j.icarus.2022.115232
Received 19 March 2022; Received in revised form 22 July 2022; Accepted 16 August 2022
Available online 28 August 2022

ocean dynamics. The combination of these two data sets provided constraints on the ice shell structure (average thickness and lateral variations, see Čadek et al. (2016, 2019) and Beuthe (2016) for Enceladus and Lefevre et al. (2014) and Kvorka et al. (2018) for Titan) which in turn can be interpreted in terms of melting/freezing at the ice/ocean interface caused by heterogeneity in the heat supplied by the buried oceans (Kvorka et al., 2018; Čadek et al., 2019).

The global scale dynamics of convecting buried oceans is a major question for the long-term evolution, the surface properties and the habitability of icy moons, yet answers are only preliminary. In a pioneering study, Soderlund et al. (2014) found latitudinal dependence of heat transfer which, in the case of Europa, may explain the preferred occurrence of specific surface features (chaos terrains, salt deposits) at mid latitudes. This latitudinal modulation of the outer boundary heat flux has been described by Yadav et al. (2016) in the more general case of rotating convection. Gastine et al. (2016) investigated thoroughly the various convective regimes simulated in a rotating spherical shell as functions of the vigor of convection and the rotation speed. In this framework, considering thinner shells appropriate for the geometry of ocean worlds, Amit et al. (2020) further showed a transition in cooling patterns: from equatorial cooling close to the rapidly-rotating regime (a feature analyzed by Miquel et al., 2018, for such shallow shells) to polar cooling (and eventually, no latitudinal dependence) closer to the non-rotating regime.

In the case of the largest icy moons such as Ganymede and Titan, radioactive decay in the rocky core alone is sufficient to maintain the presence of a buried ocean, possibly favored by anti-freeze compounds. The phase diagram of water (e.g Choukroun and Grasset, 2007, 2010) indicates that the ocean is separated from the rocky core by a thick high-pressure ice mantle, initially envisioned as a barrier to chemical exchanges. However, the detection of a significant amount of radiogenic ^{40}Ar in Titan's atmosphere implies a relatively efficient chemical transfer throughout the thick hydrosphere to the surface (Tobie et al., 2006, 2012). Indeed, numerical simulations of solid-state convection in the high-pressure ice mantle showed that heat transfer is controlled by melt production at depth and extraction of meltwater to the ocean (Choblet et al., 2017b; Kalousová et al., 2018; Kalousová and Sotin, 2018), providing an efficient way to transport chemical species from the rocky core to the ocean. The heat flux pattern through the seafloor is therefore shaped by the outlets of heat pipes of hot, partially molten ice. Interestingly for its possible influence on the melting/freezing regime of the ocean ceiling (upper ocean–ice interface), this pattern is expected to be almost permanent over tens of million years: while velocities in the high-pressure ice mantle may typically amount to a few meters per year, hot convective instabilities do not exhibit significant amounts of lateral motion over the course of a simulation (i.e. with a typical duration of 10–50 Myr).

Here, we aim to investigate how this heterogeneous seafloor heat flux pattern affects the ocean's convective flow. In order to provide a wider understanding of the phenomena at play, we consider simulations that cover different cooling patterns which may correspond to different regimes of rotating convection (Gastine et al., 2016). The prescribed heat flux at the bottom of the ocean reproduces the heterogeneous pattern exhibited at the outer boundary of 3D convection simulations in the high-pressure ice mantle (Choblet et al., 2017b). Our moderate amplitudes of heat flux heterogeneity are also chosen to reflect these results, i.e. much more modest than predicted for Enceladus, for example (Choblet et al., 2017a).

More specifically, we focus on the following questions: Is the latitudinal dependence of the heat flux at the top of the ocean affected by seafloor heterogeneity? Is there a correlation between the heat flux at the top of the ocean and the imposed seafloor heterogeneity?

In Section 2 we describe the numerical model for ocean convective flow. The results are presented in Section 3 and discussed in Section 4. We list our main conclusions in Section 5.

2. Methods

To model thermal convection in the internal oceans of Ganymede and Titan, we solve the set of hydrodynamics equations for the conservation of momentum, energy and mass for a rotating spherical shell in the Boussinesq approximation. These write, in non-dimensional form (e.g. Wicht, 2002),

$$E\left(\frac{\partial \mathbf{u}}{\partial t}+\mathbf{u}\cdot\nabla\mathbf{u}-\nabla^2\mathbf{u}\right)+2\hat{z}\times\mathbf{u}+\nabla P = Ra^*\frac{\mathbf{r}}{r_o}T, \tag{1}$$

$$\frac{\partial T}{\partial t}+\mathbf{u}\cdot\nabla T=\frac{1}{Pr}\nabla^2 T, \tag{2}$$

$$\nabla\cdot\mathbf{u}=0, \tag{3}$$

where $\mathbf{u}$ is the fluid velocity, $\hat{z}$ the direction of the rotation axis, P the pressure, $\mathbf{r}$ the radial position vector, r_o the outer boundary radius and T the temperature. Although the linear radial gravity profile in (1) may not be the most appropriate for buried oceans of icy moons, within a thin shell the gravity varies very little for any plausible radial profile (e.g. Vance et al., 2018). Here we choose this gravity profile to ease the comparison with the results of Amit et al. (2020).

Eqs. (1)–(2) are governed by three (internal) control parameters. The Ekman number represents the ratio of viscous to Coriolis forces:

$$E=\frac{\nu}{\Omega D^2}. \tag{4}$$

The Prandtl number is a ratio of diffusivities:

$$Pr=\frac{\nu}{\kappa}. \tag{5}$$

The modified Rayleigh number Ra^* represents the ratio of buoyancy vs. retarding forces. It is related to the conventional Rayleigh number Ra by $Ra^*=Ra\cdot E/Pr$, where the conventional heat flux based Rayleigh number is given by

$$Ra=\frac{\alpha g_o q_0 D^4}{\kappa\nu k}. \tag{6}$$

In (4)–(6), Ω is the rotation rate, ν the kinematic viscosity, D the shell thickness, g_o the gravitational acceleration at the outer boundary, q_0 the mean inner boundary heat flux, k the thermal conductivity and κ the thermal diffusivity. Non-dimensional time is in units of viscous diffusion time D^2/ν. In our models the heat flux is imposed from below, thus q_0 is the mean inner boundary heat flux. In the following, we explore control parameters (Table 1) that produce various cooling patterns.

In all simulations the inner to outer boundary radii ratio is set to 0.8, corresponding to a relatively thin shell compared e.g. to Earth's outer core aspect ratio of 0.35 (see Table 1 of Amit et al., 2020) and only slightly thicker compared to the aspect ratio estimates of 0.84–0.96 for the subsurface oceans of Titan (Vance et al., 2018) and Ganymede (Jara-Orué and Vermeersen, 2016). On the inner boundary, we impose a heat flux pattern (Fig. 1) based on output from simulations of high-pressure ice applied to Titan's mantle (Choblet et al., 2017b). As this interface corresponds to a phase change, prescribing a constant (melting) temperature may seem a more natural choice; in our simple framework, however, this boundary is impermeable while the most appropriate description is that of a permeable boundary (see Deguen et al., 2013, for example). As a consequence, prescribing a heterogeneous heat flux provides a way to describe the thermal influence of the high-pressure ice mantle. In our simulations, we ensure a posteriori that temperature variations along the bottom boundary are negligible. Note also that while we use the heat flux output from the solid high-pressure ice mantle as the value entering the bottom of the ocean, in reality the heat flux is expected to be discontinuous across the phase interface owing to the absorption or release of latent heat (Kvorka et al., 2018; Čadek et al., 2019). We posit that even accounting for this heat flux jump would not modify the pattern of heterogeneity which is precisely

Table 1
Models inputs and global outputs.

Model	E	Ra	$\frac{Ra_T}{Ra_c}$	q_i^*	ℓ_{max}	n_r	Re	Ro	Ro_c	$\frac{Ra}{Ra_T^{sc}}$	$\mathcal{T}$
1	1e−03	2e+05	5.05	0.57	96	49	20.63	0.021	0.45	0.63	9693
2	1e−03	2e+05	4.98	1.14	96	49	20.20	0.020	0.45	0.63	9290
3	1e−03	1e+06	11.80	0.57	96	49	53.64	0.054	1.00	3.16	5099
4	1e−03	1e+06	11.79	1.14	96	49	53.26	0.053	1.00	3.16	4823
5	3e−04	1e+07	17.70	2.00	128	73	125.92	0.038	0.95	5.20	1850
6	3e−04	5e+07	49.59	1.04	128	65	275.09	0.083	2.12	25.98	2132
7	3e−04	5e+07	47.56	2.01	128	73	275.26	0.083	2.12	25.98	1479
8	3e−04	5e+07	44.89	2.68	128	73	274.78	0.082	2.12	25.98	1313
9	3e−04	8e+07	65.33	2.00	128	73	342.59	0.103	2.68	41.57	1537
10	1e−04	1e+06	2.41	0.82	170	81	12.85	0.001	0.10	0.10	77
11	1e−04	3e+06	5.83	0.82	170	81	36.04	0.004	0.17	0.30	188
12	5e−05	1e+07	7.50	0.60	192	97	124.65	0.006	0.16	0.35	138
13	5e−05	1e+07	7.48	1.20	192	97	120.83	0.006	0.16	0.35	134
14	5e−05	1e+07	7.42	1.81	192	97	133.50	0.007	0.16	0.35	152

E is the Ekman number (4), Ra is the Rayleigh number (6), $\frac{Ra_T}{Ra_c}$ is the level of convective supercriticality for the corresponding cases with homogeneous boundary conditions, q_i^* is the amplitude of inner boundary heat flux heterogeneity, ℓ_{max} is the spherical harmonic truncation degree and order and n_r is the number of grid points in the radial direction. The number of grid points in the longitudinal and latitudinal directions n_ϕ and n_θ in our setup are related to ℓ_{max} by $n_\phi = 3\ell_{max}$ and $n_\theta = n_\phi/2$. Re is the Reynolds number (10), Ro the Rossby number (11), Ro_c the convective Rossby number (12) and $\frac{Ra}{Ra_T^{sc}}$ a ratio that represents competition between thermal and rotational boundary layers (14). $\mathcal{T}$ is the duration of the simulation in units of advection times D/U, where D is the shell thickness and U the RMS velocity amplitude in the shell.

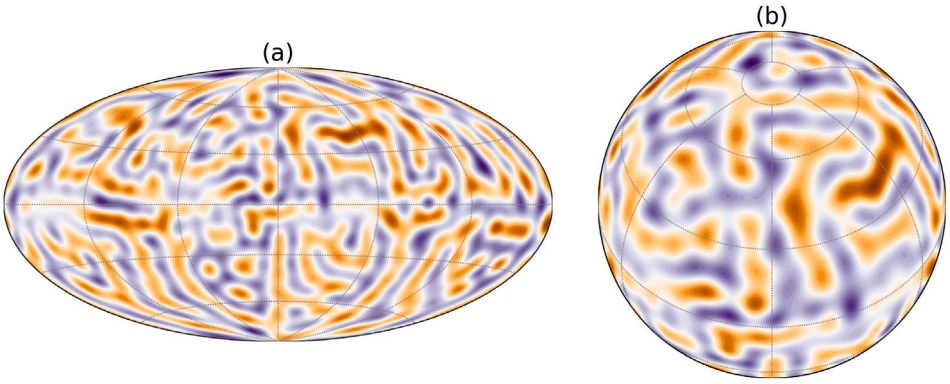

Fig. 1. Imposed pattern of inner boundary heat flux taken from the output of a high-pressure ice convection simulation applied to Titan's mantle (Choblet et al., 2017b). The heat flux is expanded up to spherical harmonic degree and order 30. (a) and (b) show different projections of the imposed heat flux pattern.

what we consider here. The amplitude of the inner boundary heat flux lateral heterogeneity is quantified by (Olson and Christensen, 2002):

$$q_i^* = \frac{q_{max} - q_{min}}{2q_0}, \tag{7}$$

where q_{max} and q_{min} are the maximum and minimum of the inner boundary heat flux, respectively. In this paper, q_i^* (where i denotes inner boundary) is an additional (boundary) control parameter. The amplitude of this heat flux heterogeneity q_i^* is limited to moderate values (i.e. order unity) between $0.57-2.68$ (see Table 1), in agreement with model predictions for the heat flux lateral variability at Titan's seafloor (Choblet et al., 2017b). Fixed temperature is set on the outer boundary, so that the heat flux there is an output of the models. On both boundaries the mechanical boundary conditions are no-slip.

Note that the imposed inner boundary heat flux (Fig. 1) corresponds to one representative snapshot from a single model of high-pressure ice applied to Titan's mantle (case 4_D^m of Choblet et al., 2017b). Obviously other high-pressure ice models with different combinations of control parameters may yield different patterns. However, our goal is to explore the extent to which the ocean dynamics alters a given bottom boundary heat flux. In that respect the pattern in Fig. 1 adequately serves our purposes and different patterns likely would not alter the main conclusions.

The convective supercriticality Ra_T/Ra_c is calculated for corresponding cases with homogeneous inner boundary heat flux ($q_i^* = 0$), where Ra_c is the critical Rayleigh number for the onset of convection and Ra_T is a temperature Rayleigh number given by (Soderlund, 2019)

$$Ra_T = \frac{Ra}{Nu}, \tag{8}$$

with Nu the Nusselt number

$$Nu = \frac{q_0 D}{k\Delta T}. \tag{9}$$

This definition of the Nusselt number ignores the effect of spherical geometry (e.g. Nu is not 1 for a conductive layer). The convective supercriticality values are given in Table 1.

Several diagnostic parameters are reported in Table 1. The ratio between inertial and viscous forces is the Reynolds number

$$Re = \frac{UD}{\nu}, \tag{10}$$

where U is the RMS velocity. The ratio between inertial and Coriolis forces is given by the Rossby number

$$Ro = \frac{U}{\Omega D} = ReE. \tag{11}$$

Following Soderlund et al. (2014) we also consider an alternative measure of inertia given by the convective Rossby number

$$Ro_c = \sqrt{\frac{RaE^2}{Pr}}. \tag{12}$$

Additionally we define a horizontal convective Rossby number

$$Ro_{cH} = \sqrt{\frac{Ra_H E^2}{Pr}}, \tag{13}$$

where $Ra_H = Raq_i^*$ (where the subscript 'H' stands for 'horizontal') reflects the convective effect of the lateral heterogeneity. As in Amit et al. (2020) we also monitor a ratio representing a competition between thermal and rotational boundary layers (King et al., 2009)

$$Ra/Ra_T^w = 0.1 RaE^{3/2} \tag{14}$$

and focusing on the inner boundary heat flux anomaly we define

$$Ra_H/Ra_T^w = 0.1 Ra_H E^{3/2}. \tag{15}$$

So far we presented parameters that characterize the global dynamics. Now we introduce parameters that characterize the pattern of outer boundary cooling. To assess whether polar or equatorial cooling governs, we follow Amit et al. (2020) and calculate the ratio between the integrated heat flux inside and outside the tangent cylinder (TC) at the outer boundary $q_o^{h/l}$ (where 'h' and 'l' superscripts stand for high and low latitudes respectively) as follows. The co-latitude where the tangent cylinder (Aurnou et al., 2003) intersects the outer boundary θ_{tc} is given by $\sin\theta_{tc} = r_i/r_o$. For $r_i/r_o = 0.8$, the TC co-latitude is $\theta_{tc} \approx 53°$. The integrated heat flux inside the TC is given by

$$q_o^h = \frac{1}{S^h}\left(\int_0^{2\pi}\int_0^{\theta_{tc}} q_o dS + \int_0^{2\pi}\int_{\pi-\theta_{tc}}^{\pi} q_o dS\right) \tag{16}$$

and outside the TC by

$$q_o^l = \frac{1}{S^l}\int_0^{2\pi}\int_{\theta_{tc}}^{\pi-\theta_{tc}} q_o dS, \tag{17}$$

where S^h and S^l denote the outer boundary spherical surface areas inside and outside the TC, respectively. Polar vs. equatorial cooling is defined by

$$q_o^{h/l} = \frac{q_o^h - q_o^l}{q_o^h + q_o^l}. \tag{18}$$

Note that here we use the full outer boundary heat flux q_o, not its anomaly δq_o, to avoid division by zero. Also note that each integral is normalized by the appropriate area so we do not calculate total fluxes but mean fluxes (or flux density). The expression (18) has some desired properties. For polar cooling it is positive, for equatorial cooling it is negative. If one of the two cooling types is much stronger it will approach plus/minus 1, whereas if the two are comparable it will approach zero.

We avoid quantifying the heterogeneous inner boundary impact on the cooling pattern by q_o^*, i.e. a quantity similar to (7) applied to the outer boundary heat flux, because unlike q_i^*, which relies on a fixed imposed pattern, q_o^* relies on local output values hence in practice it is biased by small-scale variability which might arise solely due to the finite simulation time of the runs. Amit et al. (2020) overcame this problem by computing q_o^* from latitudinal averages. However, here we cannot adopt this approach because the heterogeneous inner boundary is expected to yield longitude dependence which we wish to quantify. Instead, we decompose the outer boundary heat flux into zonal equatorially symmetric (denoted by 'zs') and non zonal equatorially symmetric (denoted by 'nzs') parts. The zonal equatorially symmetric outer boundary heat flux is given by

$$q_o^{zs}(\theta) = \left(q_o^z(\theta) + q_o^z(\pi-\theta)\right)/2, \tag{19}$$

where the 'z' superscript denotes zonal average, while the non zonal equatorially symmetric part is simply

$$q_o^{nzs}(\phi,\theta) = q_o(\phi,\theta) - q_o^{zs}(\theta), \tag{20}$$

where ϕ and θ in (19) and (20) are longitude and co-latitude, respectively. We compute the RMS values of the non zonal equatorially symmetric parts of the outer boundary heat flux anomaly $RMS(\delta q_o^{nzs})$ which is interpreted in terms of boundary control because without any boundary heterogeneity no persistent long-term deviations from axisymmetry or equatorial symmetry are expected. This is evident in e.g. Fig. 7 of Amit et al. (2020) where the long-term time-average zonal outer boundary heat flux profiles exhibit high level of equatorial symmetry even inside the tangent cylinder.

The impact of the imposed inner boundary heterogeneity on the pattern of outer boundary heat flux is further evaluated by calculating the correlation and the maximal cross-correlation between the averages of the inner and outer boundary heat flux patterns along latitude lines C_ϕ and $max(C_\phi^{cr})$, respectively. Here we focus on longitudinal dependence because latitudinal variability in the outer boundary heat flux emerges even when the inner boundary heat flux pattern is homogeneous (Amit et al., 2020) whereas long-term longitudinal variability is expected only in the presence of boundary heterogeneity. While the correlation C_ϕ quantifies the trend agreement between the inner and outer boundary heat flux patterns, the maximal cross-correlation $max(C_\phi^{cr})$ accounts for possible horizontal shifts between the imposed heat flux pattern at the bottom of the shell and the resulting heat flux at the top. Analogous shifts were reported in dynamo simulations between the imposed outer boundary heat flux pattern and the resulting time-average convection pattern (Olson and Christensen, 2002; Aubert et al., 2007; Takahashi et al., 2008).

The quantities that evaluate the boundary effect in Table 3 were computed based on the long-term time-average morphologies of the dynamical models. The averaging time of ~77-10 000 advection times is over the full simulation run (see $\mathcal{T}$ in Table 1). For comparison, Mound et al. (2019) reported an average over 37 advection times. The small-scale inner boundary heat flux pattern that we imposed (Fig. 1) likely converges slower than the commonly large-scale pattern imposed on the outer boundary in studies of Earth's core (e.g. Mound et al., 2019). Nevertheless, convergence tests using prolonged runs of cases with distinct E values and corresponding spatial resolutions indicate that the main boundary heterogeneity scale features exhibit little variations.

Table 2 indicates plausible ranges for the dimensionless parameters that characterize the subsurface oceans of Titan and Ganymede. We note that considerable uncertainties remain on most physical properties of ocean water, not only because of an uncertain composition. In addition, the ocean thickness D, or the mean basal heat flux q_0 are unconstrained.

Table 2
Plausible ranges for the dimensionless numbers for Titan and Ganymede.

	Pr	E	Ra	Ra_T	q_i^*
Titan	10	2e−12 – 5e−11	1e+25 – 1e+31	3e+20 – 5e+22	0.2 – 2
Ganymede	10	7e−13 – 3e−10	3e+27 – 4e+30	5e+18 – 1e+23	0.2 – 2

Values showed for Pr, E, Ra and Ra_T are similar to those in Soderlund (2019) (e.g. interior models values from Vance et al. (2018)). Note that the definition of the various numbers differ slightly for E and Ra, explaining the different values. In particular, the heat flux value is used in the present study to compute Ra: it is assumed to result only from radiogenic decay in the rocky interior, assumed chondritic, at present — see values in Hussmann et al. (2015). The plausible range for q_i^* is essentially unconstrained by observations: we use values obtained by models simulating convection in high-pressure ices (Choblet et al., 2017b).

3. Results

In our hydrodynamic simulations we explored the ranges $E = 1 \cdot 10^{-3} - 5 \cdot 10^{-5}$ and $Ra = 2 \cdot 10^5 - 8 \cdot 10^7$, while Pr was fixed to 1. These E values are much larger than expected for planetary conditions and likewise the Ra values are too low, as in most numerical simulations of convection in deep liquid layers (e.g. Glatzmaier, 2002). Our analysis includes representative snapshots as well as time averages. To assess dynamical regimes of simulations with non-realistic parameters, Amit et al. (2020) localized their models on the regime diagram of Gastine

Table 3
Results for the outer boundary heat flux.

Model	$q_i^{h/l}$	$q_o^{h/l}$	Cooling	RMS (δq_o^{nzs})	$\mathcal{C}_\phi$	$max\ (\mathcal{C}_\phi^{cr})$	$\mathcal{O}_2/\mathcal{I}_2$	$\mathcal{O}_{10}/\mathcal{I}_{10}$
1	0.004	−0.055	Equatorial	0.059	0.499	0.499	2.023	0.511
2	0.008	−0.051	Equatorial	0.092	0.709	0.709	2.606	0.793
3	0.004	0.011	Polar	0.094	0.571	0.585	1.545	0.520
4	0.008	0.016	Polar	0.126	0.663	0.663	1.844	0.563
5	0.016	0.024	Polar	0.210	0.717	0.734	1.907	0.640
6	0.008	0.067	Polar	0.163	0.466	0.620	1.572	0.367
7	0.016	0.072	Polar	0.184	0.520	0.675	3.964	0.941
8	0.021	0.067	Polar	0.195	0.487	0.599	4.384	0.627
9	0.015	0.078	Polar	0.174	0.480	0.630	3.964	0.644
10	0.006	−0.009	Equatorial	0.042	0.419	0.520	1.167	0.253
11	0.006	−0.035	Equatorial	0.098	0.399	0.416	2.446	0.338
12	0.010	−0.033	Equatorial	0.155	0.164	0.203	0.398	0.230
13	0.015	−0.030	Equatorial	0.152	0.417	0.421	1.129	0.325
14	0.020	−0.039	Equatorial	0.159	0.413	0.432	1.126	0.178

$q_o^{h/l}$ represents equatorial vs. polar cooling (18). $q_i^{h/l}$ is the same quantity applied to the inner boundary using the same latitude limits. $RMS(q_o^{nzs})$ is the integrated non zonal symmetric heat flux (20) which represents the impact of the boundary heterogeneity. $\mathcal{C}_\phi$ and $max(\mathcal{C}_\phi^{cr})$ are the correlation and the maximum of the cross-correlation coefficients, respectively, between inner and outer boundary heat flux averaged along longitude lines. $\mathcal{O}_2/\mathcal{I}_2$ and $\mathcal{O}_{10}/\mathcal{I}_{10}$ are the outer/inner boundary ratio of non-dimensional heat flux power for order 2 and 10, respectively.

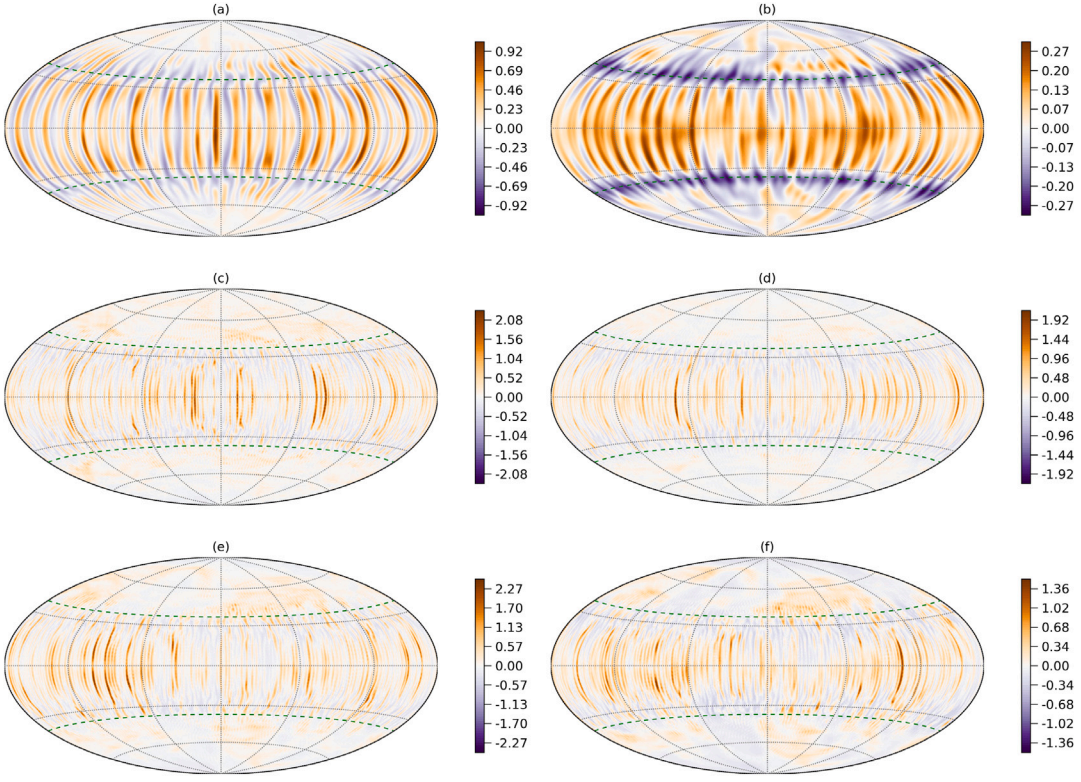

Fig. 2. Outer boundary heat flux anomalies in snapshots (left) and time-averages (right) for cases 1 (a,b), 12 (c,d) and 14 (e,f) which are characterized by equatorial cooling. Dashed latitude lines denote the tangent cylinder. Note the different color scales.

et al. (2016). However, such regime diagrams depend on Ra and E exclusively (Gastine et al., 2016; Long et al., 2020), while the little explored impact of q_i^* (which may vary depending on the particular imposed heat flux pattern) is absent in these diagrams. Since the main control parameters are roughly similar in our study and that of Amit et al. (2020) with homogeneous boundary conditions, we compare our findings with those of Amit et al. (2020) and assess the impact of the boundary heterogeneity in Section 5.

3.1. Polar vs. equatorial cooling

Competing effects of rotation and convection control the large-scale pattern of outer boundary heat flux (see Amit et al., 2020, and references therein). Larger role of rotation effects leads to larger heat flux at low latitudes, whereas polar cooling emerges when convection is increased. Our outer boundary heat flux patterns encompass these two endmember dynamical regimes. Figs. 2 and 3 show outer boundary heat flux anomaly distributions of our hydrodynamic models with equatorial and polar cooling, respectively.

The equatorial cooling patterns seen in Fig. 2 are characterized by low- and mid-latitude strips oriented in the north–south direction. Such invariance in the direction of the rotation axis indicates dominance of rotational effects (e.g. Busse, 1970). These strips are not evenly distributed in longitude, especially in cases with stronger amplitude of imposed boundary heterogeneity or/and stronger main convection vigor. For the snapshots in Fig. 2, this longitudinal preference points to a possible consequence of either statistical preference due to boundary

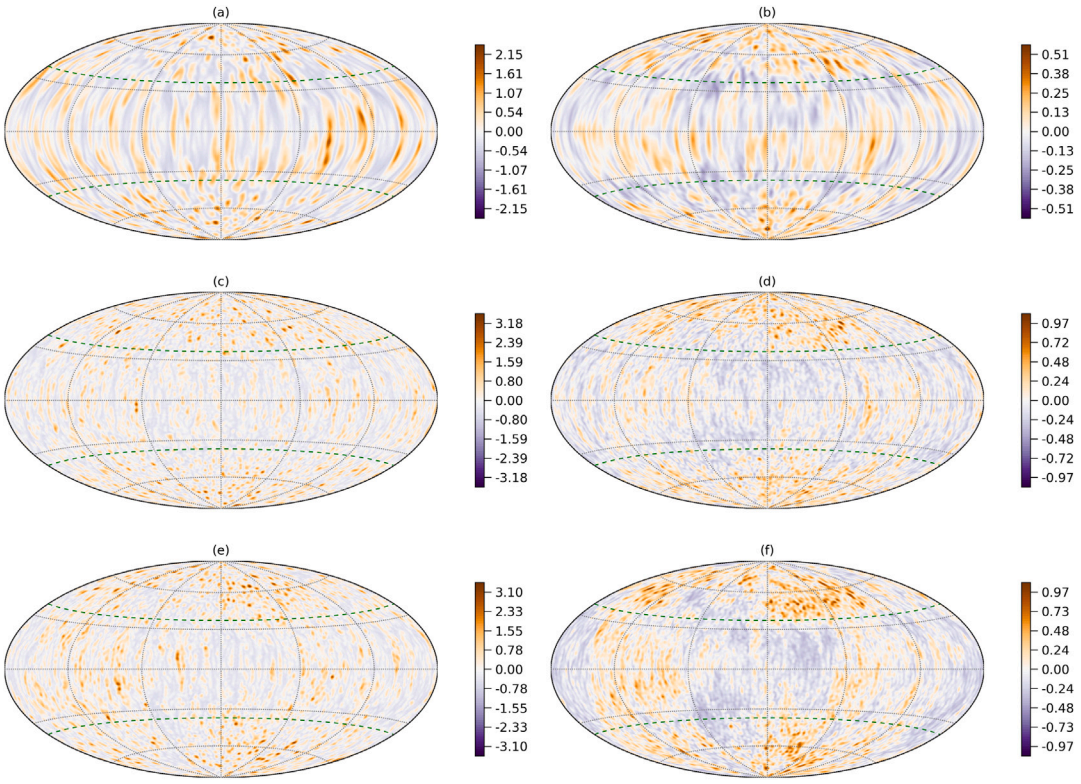

Fig. 3. As in Fig. 2 for cases 3 (a,b), 6 (c,d) and 8 (e,f) which are characterized by polar cooling.

control or time-dependent chaotic convection. The latitude extent of the strips roughly reaches the edge of the TC (latitudes 37° in our models' setup), though in some longitudes the meridional heat flux strips penetrate the TC. In models with increasing effects of rapid rotation (i.e. smaller Rossby numbers) these strips become increasingly thinner (compare Figs. 2a and b vs. 2c and d). Increasing amplitude of imposed inner boundary heterogeneity leads to destruction of some north–south strips (compare Figs. 2c and d vs. 2e and f). Some weaker heat flux anomalies inside the TC nevertheless appear in both snapshots and time averages of cases with equatorial cooling. On time averages, pronounced negative heat flux anomaly belts appear at the edges of the TC. As q_i^* increases from case 12 to 14, positive heat flux anomalies become more pronounced, especially inside the TC (compare Fig. 2d and f).

The polar cooling patterns seen in Fig. 3 are characterized by stronger high-latitude positive heat flux anomalies. The time-averages show more clearly that the high-latitude positive heat flux anomalies exceed the equatorial positive anomalies (also see positive $q_o^{h/l}$ for these cases in Table 3). Our cases 5–9 with the highest values of Ra_H are characterized by polar cooling and lack any coherent north–south strips in their outer boundary heat flux patterns. Instead, small-scale circular features characterize the instantaneous outer boundary heat flux. These high-latitude patches roughly extend until the edge of the TC.

To further illustrate the differences between polar and equatorial cooling, Fig. 4 compares polar and equatorial views of the outer boundary heat flux anomalies for case 12 (Fig. 4a and b) characterized by equatorial cooling vs. case 7 (Fig. 4c and d) characterized by polar cooling. As mentioned above, for models with stronger convection characterized by polar cooling the low-latitude north–south strips fade (Fig. 4c) and small-scale heat flux structures emerge at high latitudes inside the tangent cylinder (Fig. 4d). When rotation effects dominate, high-latitude positive anomalies are weaker and the heat flux is governed by north–south elongated strips outside the TC.

The latitude dependence of the imposed inner boundary heat flux is shown in Fig. 5 (blue curve). This latitudinal dependence is an outcome of a solid-state convection simulation in the high-pressure ice mantle, which includes no rotational (hence latitudinal) effect. In addition, the heat distribution is homogeneous in this model as tidal heating in the high-pressure ices and the rocky core is expected to be a very minor contribution and neglected in the simulation. Therefore there is a priori no reason for the imposed inner boundary heat flux pattern to contain a marked latitude dependence other than fortuitous. As its power spectrum peaks at relatively large spherical harmonic degrees ($\ell \simeq 20$; Choblet et al., 2017b), the average along longitude lines is expected to display modest largest-scale variability. Yet, somewhat incidentally it contains a rather substantial level of equatorial symmetry (red curve in Fig. 5). In contrast, as expected the integrated heat flux inside and outside the TC are rather comparable, albeit slightly more polar (see positive weak $q_i^{h/l}$ values in Table 3).

Fig. 6 presents the latitude dependence of the time-averaged outer boundary heat flux patterns. The models are classified into two groups depending on the dominating cooling pattern (see Table 3). Cases dominated by equatorial cooling (negative $q_o^{h/l}$ in Table 3) are shown in Fig. 6a, whereas cases dominated by polar cooling (positive $q_o^{h/l}$ in Table 3) are shown in Fig. 6b. Fig. 6a highlights three characteristics of our equatorial cooling cases: positive anomalies at low latitudes with peaks at the equator, negative anomalies at high-latitudes with lows at the poles and pronounced negative heat flux anomalies at the edges of the TC. A somewhat simpler pattern of positive/negative anomalies inside/outside the TC respectively appears in the polar cooling cases (Fig. 6b).

The dynamical origin of the latitudinal distribution of outer boundary heat flux is presented in Fig. 7. In the equatorial cooling case, the flow consists of thin axial columns outside the TC which are invariant along the direction parallel to the rotation axis (Fig. 7a and c), typical to rapidly rotating flows (e.g. Busse, 1970; Olson et al., 1999; Gastine et al., 2016; Long et al., 2020). In contrast, the radial velocity in a snapshot of the polar cooling case exhibits a 3D morphology (Fig. 7b and d) characteristic of inertial effects driven by vigorous convection. The zonal velocity profiles emphasize that indeed the convective activity in

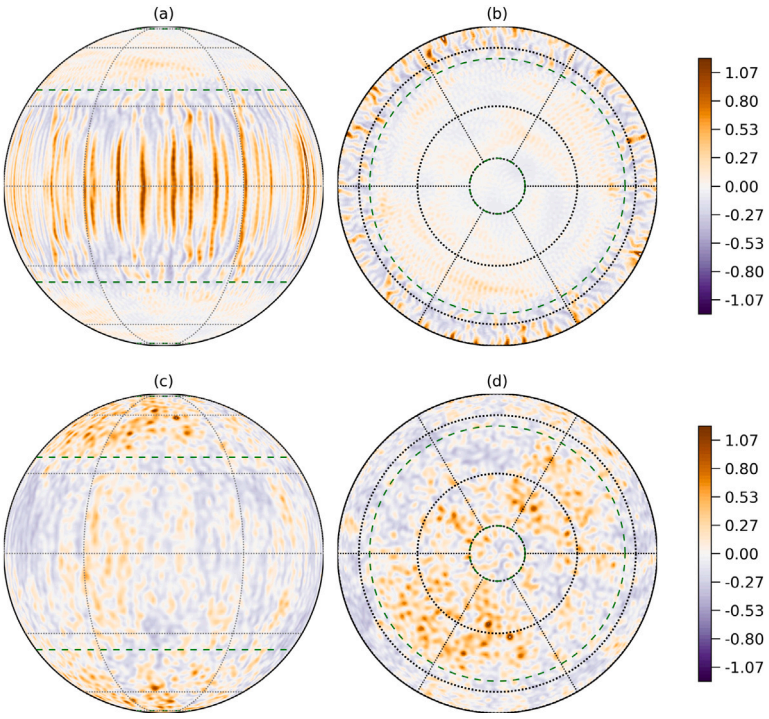

Fig. 4. Equatorial (left) and North polar (right) views of the time-averaged outer boundary heat flux anomalies for cases 12 (a,b) characterized by equatorial cooling and 7 (c,d) characterized by polar cooling. Dashed latitude lines denote the tangent cylinder.

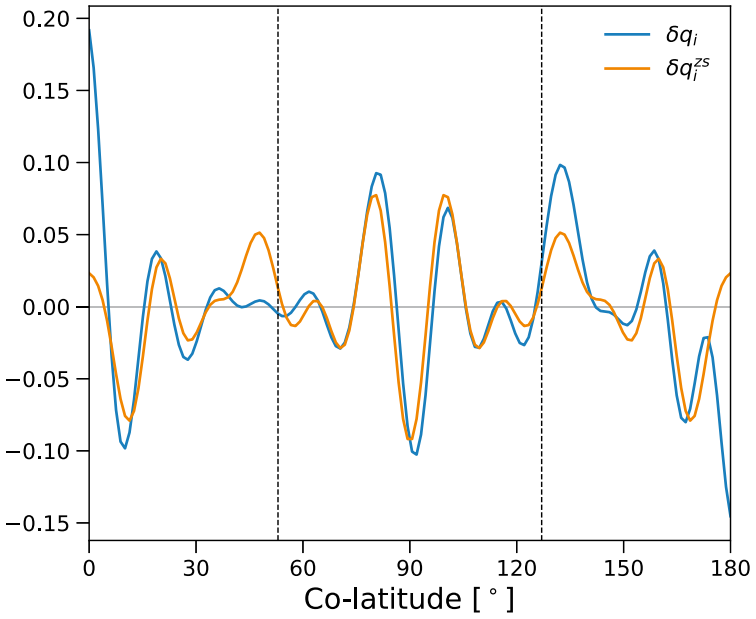

Fig. 5. Imposed inner boundary heat flux anomaly averaged along latitude lines (blue) and its equatorially symmetric part (red) vs. co-latitude. Vertical lines denote the tangent cylinder.

the polar cooling case is concentrated in the polar regions (Fig. 7d) whereas in the equatorial cooling case the axial columns efficiently transfer heat from the inner to the outer boundary at low and mid latitudes (Fig. 7c).

3.2. Impact of boundary heterogeneity

Next we investigate the relation between the patterns of inner and outer boundary heat flux anomalies. Comparison of Fig. 1 with Figs. 2 and 3 shows traces of local boundary control in the form of regions of strongest heat flux on the outer boundary corresponding to most intense imposed heat flux on the inner boundary, see e.g. the features 60° east of the central meridian inside the TC. This is best seen on long-term time averages (especially in Figs. 2f and 3f). Indeed such a projection of the inner boundary heat flux pattern onto the outer boundary is expected for a thin shell, large amplitude of imposed inner boundary heterogeneity and larger role of convection vs. rotation in the dynamics. Stronger rotational effects are expected to smear latitudinal variability outside the TC but would still favor preferred longitudes where axial columns would expel more heat flux through the outer boundary (Fig. 2d and f). There is a hint of such a relation even

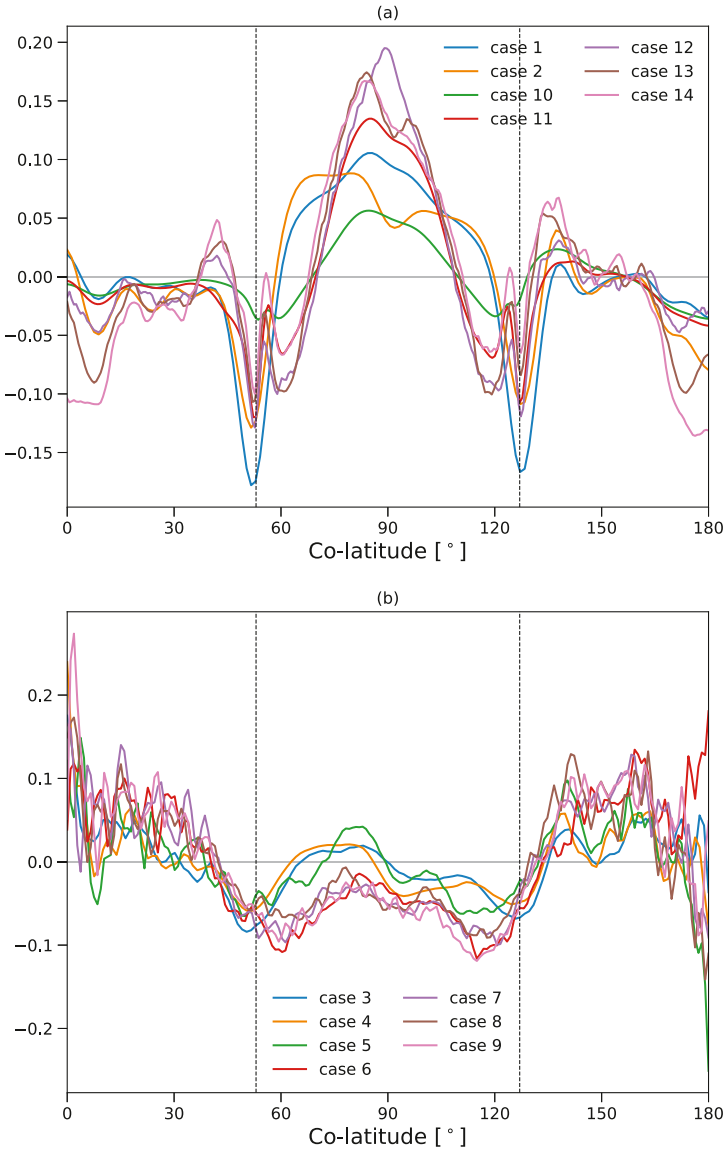

Fig. 6. Outer boundary heat flux anomaly averaged along latitude lines vs. co-latitude. Vertical lines denote the tangent cylinder. Equatorial and polar cooling cases are shown in (a) and (b) respectively.

when comparing the latitude dependence, for example the asymmetry between the positive/negative inner boundary heat flux anomaly in the North/South pole respectively (Fig. 5) appears also in most models (especially in the polar cooling cases) on the outer boundary (Fig. 6b).

We now focus on the longitudinal distributions of the time-averaged outer boundary heat flux which are expected to be uniform in the absence of boundary heterogeneity (Olson and Christensen, 2002; Amit et al., 2015). We compare these model outputs with the imposed inner boundary heat flux averaged along longitude lines (Fig. 8).

Fig. 9 presents the outer boundary heat flux averaged along longitude lines of the hydrodynamic models. Here we classified the models according to their correlation coefficient C_ϕ. Common to all cases is the dominance of the short wavelength that characterizes the inner boundary heat flux pattern (Fig. 8). The correlation coefficient seems to decrease with decreasing E (from Fig. 9a to 9c), though this might be due to shorter averaging times for our lower E cases (Table 1). In addition, outer boundary heat flux patterns of some models contain a large-scale order 2 signal (Fig. 9b). This order 2 pattern is particularly evident in the polar regions of polar cooling cases 5–9 (see e.g. Figs. 3d, f and 4d) and also (to a lesser extent) at low latitudes of the equatorial cooling cases (e.g. Fig. 2f). Indeed, the outer boundary heat flux power of order 2 is amplified with respect to the inner boundary heat flux of the same order in almost all cases (Table 3), with the largest amplification in the polar cooling cases (Fig. 10). For comparison, the peak power of inner boundary heat flux at order 10 actually becomes weaker at the outer boundary for all cases (Table 3). We elaborate on the origin of the large-scale order 2 pattern in the Discussion.

For a more quantitative analysis we calculated the correlation and the maximum cross-correlation coefficients C_ϕ and $max(C_\phi^{cr})$, respectively, between the longitude-averaged outer vs. inner boundary heat flux (Table 3). The $max(C_\phi^{cr})$ coefficients account for possible azimuthal shifts between the inner and the outer boundary heat flux patterns. In all cases the correlation is positive and statistically significant. Based on the student's t-test (Press et al., 1989), for the spatial resolution of our models (Table 1), a level of 95% statistical significance corresponds to a global spatial correlation of about 0.2 (Rau et al., 2000). In all cases except case 12 C_ϕ exceeds 0.2, while $max(C_\phi^{cr})$ exceeds 0.2 in all cases, indicating clear boundary control on the outer boundary heat flux. The largest values of C_ϕ and $max(C_\phi^{cr})$ are found for polar cooling case 5 and the smallest for equatorial cooling case 12. In general, models with polar cooling patterns show larger correlation improvement from C_ϕ to $max(C_\phi^{cr})$.

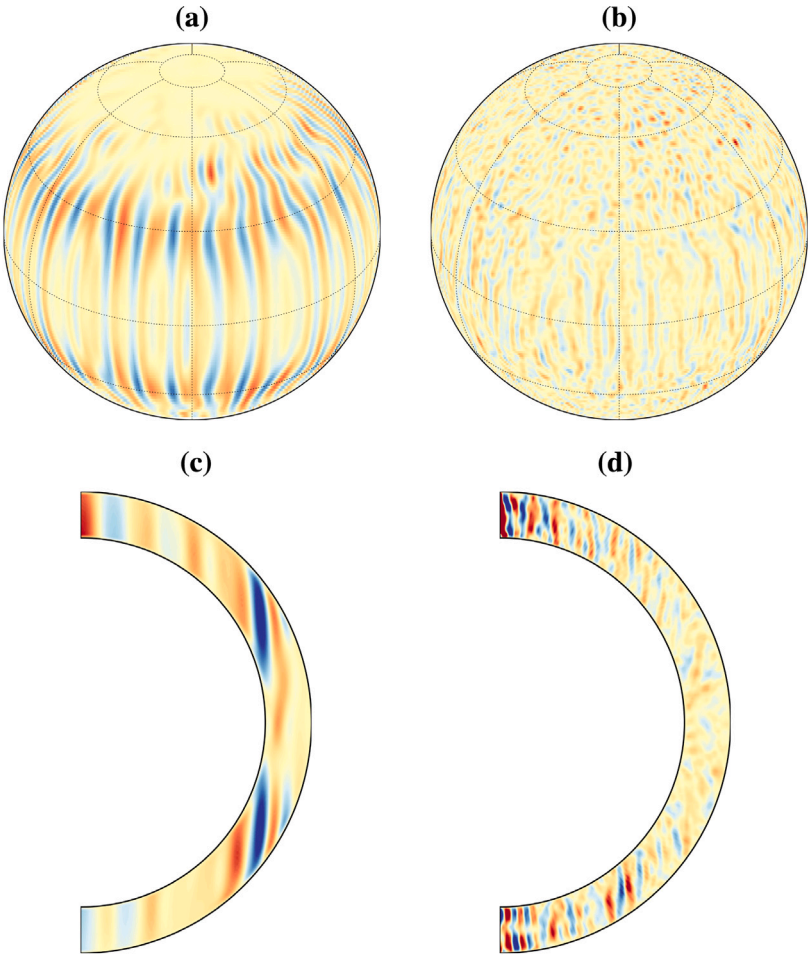

Fig. 7. Non-dimensional radial velocity in snapshots of cases 2 (left; equatorial cooling) and 7 (right; polar cooling) just below the Ekman boundary layer (top) and at zonal averages (bottom).

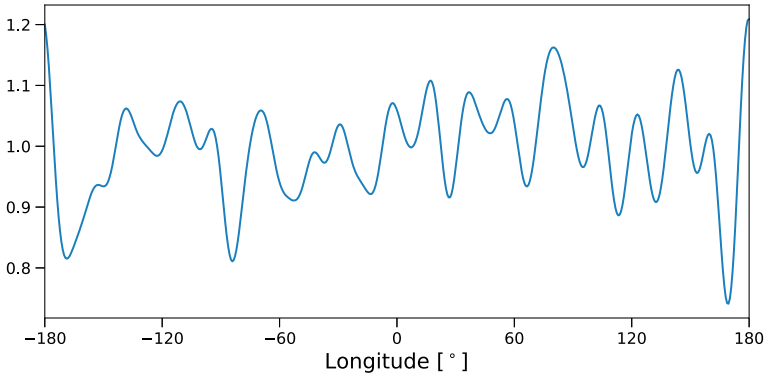

Fig. 8. Inner boundary heat flux averaged along longitude lines vs. longitude.

We note that the low-latitude positive heat flux anomalies are somewhat larger in the northern hemisphere, as can be seen in the latitudinal profiles (Fig. 6). This is due to the slightly larger imposed inner boundary heat flux at low-latitudes of the northern hemisphere (Fig. 5). Obviously this north–south asymmetry is just pure chance — there is no physical reason for any hemispherical preference in the pattern of the inner boundary heat flux. We merely point here that this slight imposed hemispherical asymmetry is reflected in the resulting outer boundary heat flux.

3.3. Dependence on control parameters

It is important to note that the cooling type (equatorial or polar) is not affected by the amplitude of the inner boundary heterogeneity. Our models exhibit the same type of cooling patterns for different q_i^*. However, the amplitude of the cooling pattern is strongly affected by the boundary heterogeneity. In addition, the dependence of the cooling pattern on the internal control parameters (i.e. E and Ra) is also modified by the boundary heterogeneity.

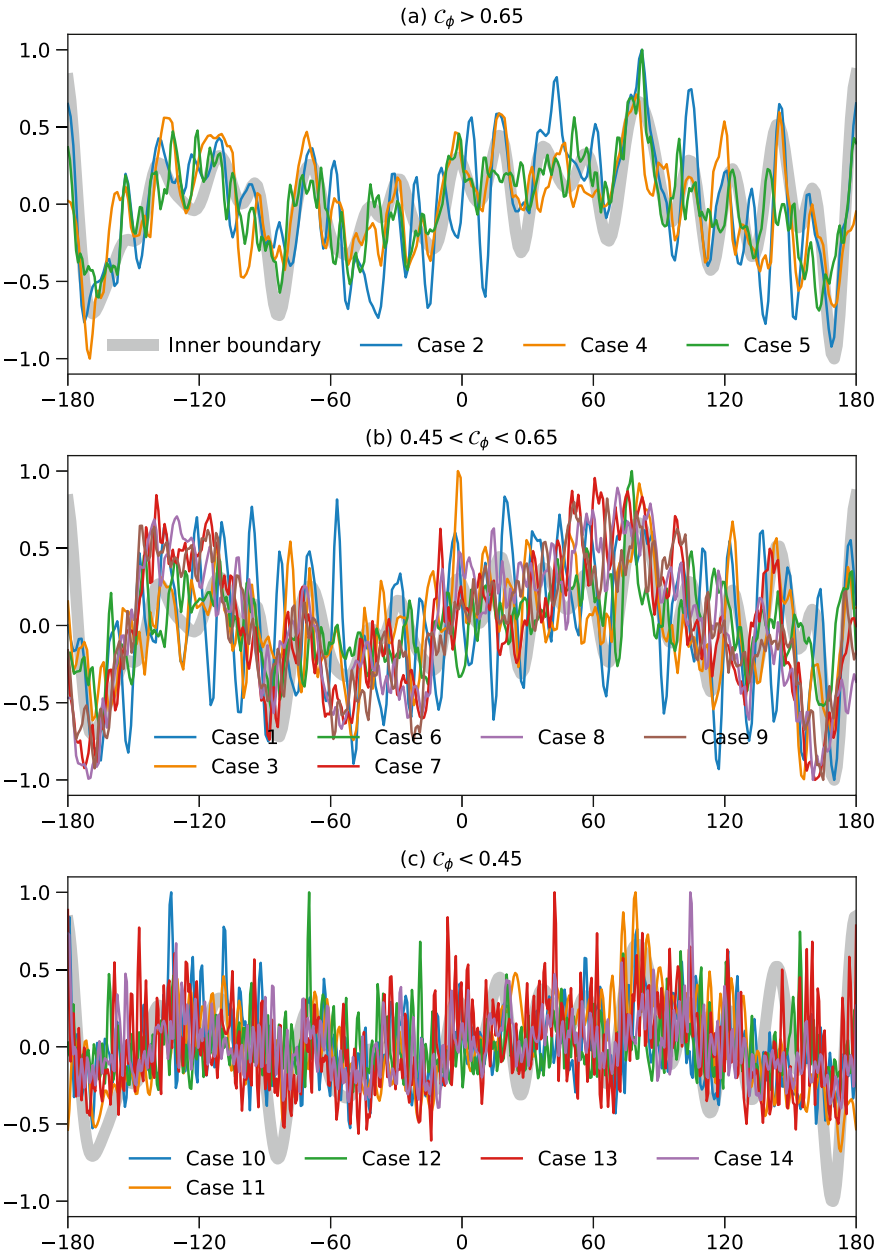

Fig. 9. Outer boundary heat flux anomaly averaged along longitude lines vs. longitude. Thick gray lines represent inner boundary heat flux.

We now turn to examine the dependence of our measure of polar vs. equatorial cooling $q_o^{h/l}$(18) on the level of inertia in the system (Soderlund et al., 2014; Amit et al., 2020). We test the dependence of this quantity on the ratios representing competitions between thermal and rotational boundary layers Ra_T/Ra_T^w (as in (14) but based on the temperature Rayleigh number) and Ra_H/Ra_T^w(15), the latter capturing the convective effect of the inner boundary heat flux heterogeneity. The results are displayed in Fig. 11. In our models $q_o^{h/l}$ depends not only on the competition between rotation and convection (Amit et al., 2020) but also on the amplitude of the inner boundary heterogeneity q_i^*. Nevertheless, Fig. 11a shows that equatorial/polar cooling patterns characterized by negative/positive $q_o^{h/l}$ correspond to lower/higher Ra_T/Ra_T^w, respectively, in qualitative agreement with the main results of Amit et al. (2020) for homogeneous boundary conditions (see red symbols in Fig. 11a), i.e. stronger inertial effects lead to polar cooling whereas rotational effects promote equatorial cooling. Also in agreement with Amit et al. (2020), our cases with $Ra_T/Ra_T^w < 1$ are classified as equatorial cooling, whereas our cases with $Ra_T/Ra_T^w > 1$ are characterized by polar cooling. However, our absolute $q_o^{h/l}$ values are significantly smaller than those obtained by Amit et al. (2020). In addition, our $q_o^{h/l}$ values for the equatorial cooling cases slightly decrease with increasing Ra_T/Ra_T^w (Fig. 11a). These discrepancies are inevitably attributable to the imposed heterogeneous inner boundary heat flux in our simulations, but also to the lower Rossby numbers models that we studied compared to the models of Amit et al. (2020) and Kvorka and Čadek (2022). However, accounting for q_i^* practically does not modify the qualitative dependence of $q_o^{h/l}$ on the measure of inertia (Fig. 11b).

Next in Fig. 12, we explore the dependence of the amplitude of the non zonal equatorially symmetric part of the outer boundary heat flux anomaly on the control parameters. This component of the heat flux is expected to arise solely due to the imposed inner boundary heterogeneity. Therefore, a natural candidate for the amplitude of the deviations of the outer boundary heat flux from axisymmetry and equatorial symmetry is the horizontal Rayleigh number Ra_H (e.g. Willis et al., 2007; Monteux et al., 2015). Fig. 12 indeed suggests that

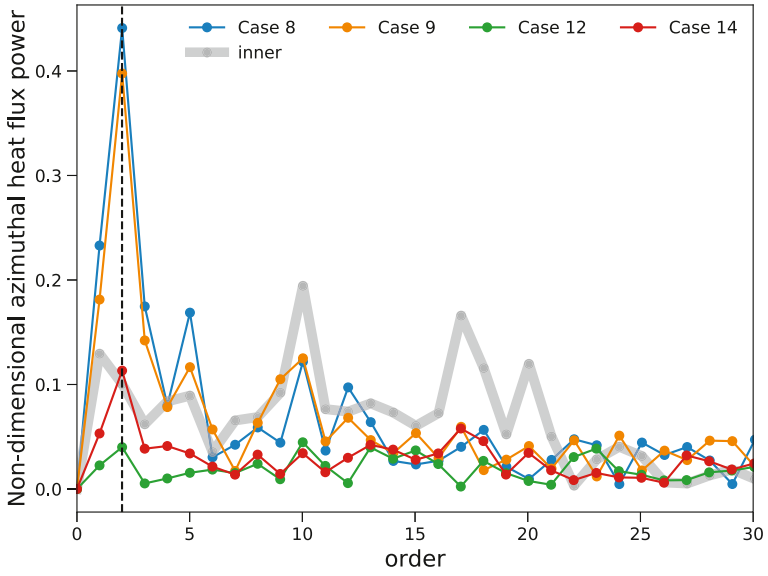

Fig. 10. Non-dimensional time-average azimuthal heat flux power of outer (colors) and inner (thick gray) boundary heat flux for four selected models, vs. order. The largest (blue and orange) and the smallest (red and green) amplifications of order 2 among the studied cases are shown.

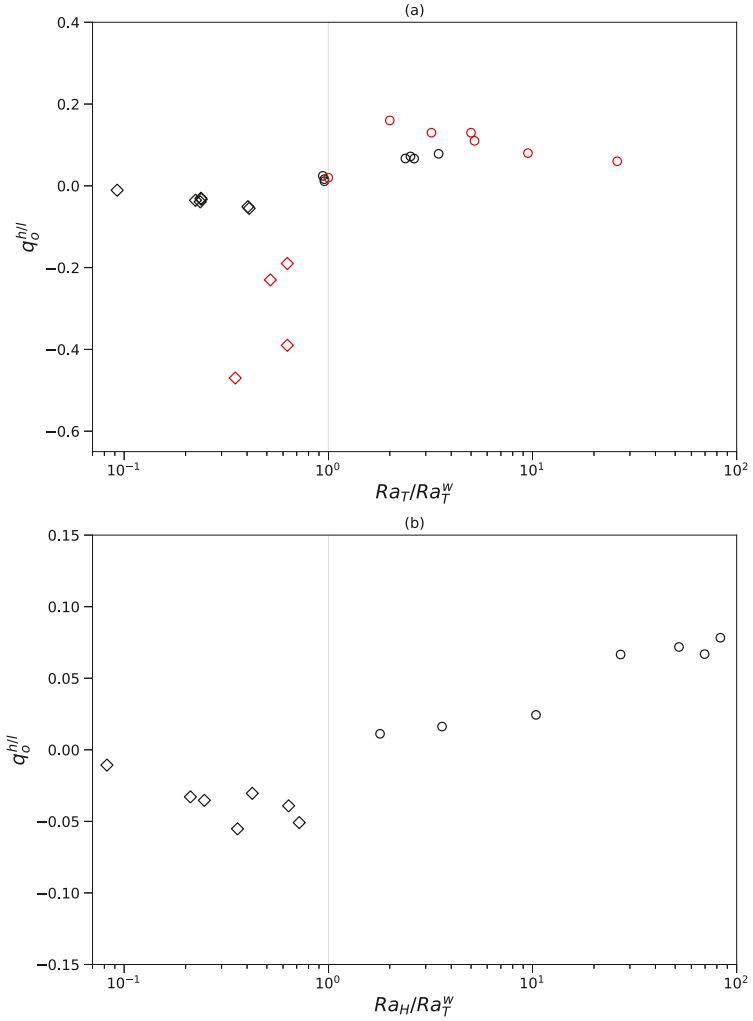

Fig. 11. $q_o^{h/l}$ vs. Ra_T/Ra_T^w (a) and Ra_H/Ra_T^w (b). Diamonds/Circles represents equatorial/polar cooling patterns, respectively. Red symbols in (a) are the results from Amit et al. (2020). Note that in (a) the temperature Rayleigh number Ra_T is used for comparison with the models of Amit et al. (2020), whereas in (b) the flux Rayleigh number Ra is used.

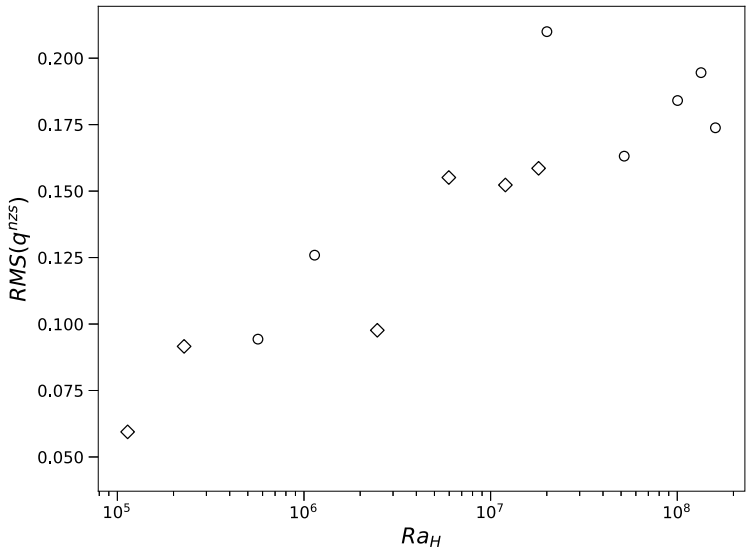

Fig. 12. $RMS(\delta q_o^{nzs})$ vs. Ra_H. Diamonds/Circles represent equatorial/polar cooling patterns, respectively.

increasing Ra_H results in larger deviations from axisymmetry and equatorial symmetry caused by the imposed inner boundary heterogeneity. Attempts to explain δq_o^{nzs} with Ra or q_i^* are much less satisfactory, and the same holds with Ra_H/Ra_T^w (not shown).

For a single spherical harmonic imposed boundary condition, the order of the time-average convection pattern follows that of the imposed boundary condition, though a phase shift is possible (Olson and Christensen, 2002; Aubert et al., 2007; Takahashi et al., 2008). When multi-harmonic boundary conditions are used, as in our case, convective mixing may lead to a more complex pattern distortion. Analogous to Fig. 11, in Fig. 13 we explore the dependence of the correlations between the patterns of outer and inner boundary heat flux C_ϕ and $max(C_\phi^{cr})$ on Ra_H/Ra_T^w. Two branches are seen in Fig. 13. One branch associated with equatorial cooling cases and polar cooling cases with relatively low Rossby numbers exhibits large reduction in correlation for small decrease in Ra_H/Ra_T^w, whereas another branch associated entirely with polar cooling cases exhibits very weak reduction in correlation for changes in Ra_H/Ra_T^w. In addition, in models occupying the latter branch a more significant improvement in correlation appears when allowing for azimuthal shifts (compare Fig. 13a and b). Below we interpret these trends in terms of different dynamical regimes.

4. Discussion

We classified the latitudinal profiles of outer boundary heat flux into two types of cooling patterns: equatorial and polar (Fig. 6 and Table 3). Amit et al. (2020) found that large inertia favors polar cooling whereas weak inertia leads to equatorial cooling. We find that $q_o^{h/l}$, our measure of polar vs. equatorial cooling, depends on inertia in a similar way. Our polar cooling cases are systematically characterized by larger effective Rossby numbers than our equatorial cooling cases. However, the absolute $q_o^{h/l}$ values in our models are significantly lower than those obtained by Amit et al. (2020) with homogeneous boundary conditions and similar effective Rossby numbers (Table 3 and Fig. 11a). Because the imposed inner boundary heterogeneity has comparable heat flux partitioning at the latitude ranges that correspond to inside and outside the TC intersection with the outer boundary (Fig. 5) as expected from solid convection simulations with no preferred latitude, it tends to reduce the latitudinal variability of the heat flux. Therefore, the resulting cooling pattern is less variable in latitude than that obtained with homogeneous boundary conditions (Fig. 11a). The extent of this reduction depends on the amount of zonal symmetric heat flux. The pattern imposed in this study contains a significant amount of zonal equatorial symmetry (Fig. 5). If projected to the outer boundary it would produce a close to balanced heat flux inside and outside the TC. Competing effects of boundary heterogeneity and internal control parameters hence lead to considerable reduction in the absolute values of $q_o^{h/l}$ (Fig. 11a). This trend persists even when incorporating q_i^* in the scaling law using Ra_H/Ra_T^w (Fig. 11b).

The decrease in $q_o^{h/l}$ with increasing Ra_T/Ra_T^w in our equatorial cooling cases arises from the low Rossby numbers of these models which reside in the weakly non-linear parametric regime (Gastine et al., 2016) which was not explored by Amit et al. (2020) and Kvorka and Čadek (2022). In the weakly non-linear regime, decreasing Rossby numbers approach the onset of convection and uniform latitudinal dependence of heat flux. In Fig. 11b there is a change in trend within the equatorial cooling cases at $Ra_H/Ra_T^w \sim 0.3$. For larger Ra_H/Ra_T^w values $q_o^{h/l}$ increases with increasing Ra_T/Ra_T^w values, as in the homogeneous boundary condition models (Amit et al., 2020; Kvorka and Čadek, 2022). This value of $Ra_H/Ra_T^w \sim 0.3$ probably marks the limit between the weakly non-linear and transitional regimes for the pattern of inner boundary heat flux used in our study.

In all our models we set $Pr = 1$, which corresponds to a turbulent Prandtl number. This choice is motivated for comparison purposes with numerous previous studies (e.g. Gastine et al., 2016; Soderlund, 2019; Amit et al., 2020). However, in subsurface icy moons $Pr = 10$. Kvorka and Čadek (2022) explored the dependence of the heat transfer in rotating convecting thin spherical shells on Pr. They found for all Pr values that increasing effective Rossby numbers lead to a transition from equatorial to polar cooling and then back to equatorial cooling, in qualitative agreement with the results of Amit et al. (2020). However, the peak level of polar cooling and the effective Rossby numbers at which it occurs depend on Pr (Kvorka and Čadek, 2022). It is therefore plausible that our results with a heterogeneous inner boundary heat flux may depend on Pr.

Polar vs. equatorial cooling is linked to the role of strong zonal jets in the dynamics. Coriolis force deflects westward flow towards the rotation axis. Therefore at the equator zonal jets quench low-latitude radial flows and sweep thermal structures there hence leading to polar cooling (Aurnou et al., 2008; Yadav et al., 2016), in contrast to the resulting spiraling motion at polar regions (Olson and Aurnou, 1999; Cao et al., 2018). Furthermore, Yadav et al. (2016) found that the increase in heat transfer with increasing Rayleigh number is much stronger in the polar regions than in the equatorial region. In addition, the amplitude of the zonal jets depends on the Rossby number in a non-monotonic way (Yadav et al., 2016). These issues may pose problems

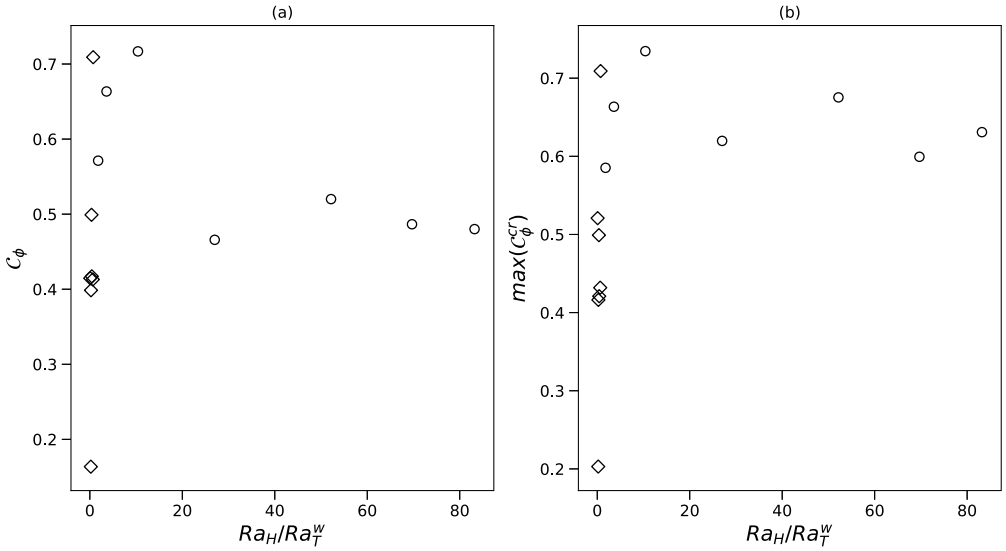

Fig. 13. Correlations between outer and imposed inner boundary heat flux patterns vs. Ra_H/Ra_T^w (15). In (b) possible azimuthal shifts are accounted for. Diamonds/Circles represents equatorial/polar cooling patterns, respectively. Note slightly different y-axis scales in (a) vs. (b).

in isolating the role of inner boundary heterogeneity in the latitudinal distribution of outer boundary heat flux.

The heterogeneous inner boundary heat flux leads to deviations from axisymmetry and equatorial symmetry. Above regions of high imposed inner boundary heat flux, plumes develop and carry more heat efficiently to the outer boundary. Consequently, these patches of high inner boundary heat flux project high heat flux at the same regions on the outer boundary, especially in models with large amplitude of inner boundary heterogeneity q_i^* (Figs. 1–3). Such a correlation is particularly expected when the shell is thin, q_i^* is large and convective effects dominate over rotational. More dominant rotational effects reduce the boundary effect outside the TC.

All models show a slight tendency of positive outer boundary heat flux towards the low latitudes of the northern hemisphere (Fig. 6), as in the imposed inner boundary heat flux pattern (Figs. 1 and 5). Far more importantly, preferred longitudes of positive outer boundary anomalies are evident in the maps (Figs. 2–3) and in particular in the longitude averages (Fig. 9) of all models. The outer boundary heat flux longitude dependence is highly correlated with the inner boundary pattern (Fig. 9 and Table 3). The correlations degrade when more rapid rotation and weaker boundary heterogeneity are considered (Fig. 9 and Table 3). This correlation reduction follows two distinctive branches, both incorporated in the horizontal effective Rossby number Ra_H/Ra_T^w (Fig. 13). In equatorial and polar cooling cases with relatively low Rossby numbers, both of which appear in the dynamical transitional regime (Gastine et al., 2016) but close to the weakly nonlinear regime (Amit et al., 2020), according to the scaling laws in this regime, the convective length scale (i.e. the thickness of the axial columns) decreases with decreasing Ekman number E (Aubert et al., 2001; King and Buffett, 2013; Gastine et al., 2016). These thinner axial convective columns lead to stronger pattern distortion by convective mixing and thus reduction in correlation between the inner and outer boundary heat flux spatial distributions. In contrast, in polar cooling cases with relatively large Rossby numbers which also appear in the dynamical transitional regime (Gastine et al., 2016) but close to the non-rotating regime (Amit et al., 2020), obviously rotation does not play a major role; here weaker boundary heterogeneity q_i^* results in weaker boundary control and hence lower correlations. We find that the correlation reduction due to this latter effect is much weaker. In addition, improved cross-correlations are more prominent in the polar cooling cases.

An intriguing feature of our results which is visible in the longitude-dependent profiles of the outer boundary heat flux of some models (Fig. 9) is the emergence of a large-scale order 2 pattern, most notably in the polar cooling cases. The signature of this order 2 part in the imposed boundary condition is weak, though it exists; note that the order 2 peaks on the outer boundary (Fig. 9) coincide with inner boundary peaks (see Fig. 8). This weak imposed large-scale heterogeneity is amplified by convection across the thin shell. Convection may mix and hence filter small scales, i.e. enhance (relatively) large scales. Aubert et al. (2008) obtained an order 1 pattern of co-density flux on the inner boundary from an imposed tomographic (i.e. dominantly order 2) pattern on the outer boundary of their geodynamo models. This filtering of small scales by mixing appears when convection is sufficiently vigorous; when convection is closer to onset, the imposed boundary heterogeneity is maintained on the other boundary (Gubbins et al., 2011).

The boundary control effect is further quantified by the part of the outer boundary heat flux that is non zonal symmetric. This part increases with increasing horizontal Rayleigh number Ra_H (Fig. 12), i.e. stronger mean convection and larger amplitude of imposed heat flux heterogeneity lead to more longitude dependence and possibly more deviations from equatorial symmetry in the resulting outer boundary heat flux.

Our models span different values of E, Ra and q_i^*, but we use a fixed $Pr = 1$ value in all cases. In addition, we use no-slip mechanical boundary conditions in all simulations, while under free-slip conditions rapid rotation may yield strong zonal flows which in turn may sweep the equatorial heat flux and favor polar cooling (Aurnou et al., 2008; Yadav et al., 2016). We also neglect all convective effects related to salts (buoyancy due to their crystallization or melting). Caution should thus be taken in the interpretation of the results and the projections to the icy moons since any result may additionally depend on the Pr value, the type of mechanical boundary condition or possibly the impact of salts on the convection.

Our results may have implications to the relations between different layers at the interior of icy moons. We hypothesize two main large-scale characteristics of the heat flux at the top of the subsurface oceans. First, polar cooling (Amit et al., 2020). Second, a dominant large-scale (order 2 in the case of the particular imposed pattern used here) longitude dependence. Moreover, can the heat flux at the bottom of the subsurface ocean be inferred from surface observations? Our results show that the outer boundary heat flux pattern is related to the imposed inner boundary heat flux pattern but some distortion may prevail. In addition, the top icy layer may further modulate the signal from the top of the ocean to the surface.

5. Conclusions

There are two differences between our models and those of Amit et al. (2020), both concern the inner boundary thermal condition. First, Amit et al. (2020) set a fixed temperature whereas we set a fixed heat flux. Second, their inner boundary temperature is homogeneous whereas our heat flux is laterally varying. Although the amplitude of imposed inner boundary heat flux heterogeneity in our models is rather moderate ($q_i^* < 3$, see Table 1), several important results arise from this heterogeneity:

- Persistent preferred longitudes of intense outer boundary heat flux are highly correlated with longitudes of intense inner boundary heat flux. For the equatorial cooling cases, this correlation decreases strongly with increasing rotation rate. In contrast, for the polar cooling cases, the correlation decreases weakly with decreasing amplitude of inner boundary heterogeneity.
- In addition, a non-trivial large-scale order 2 pattern is amplified by the convection in the thin shell, which may have a positive retroaction on the dynamics of the high-pressure ice mantle.
- Deviations from axisymmetry and equatorial symmetry in the outer boundary heat flux increase with the horizontal Rayleigh number which contains the amplitude of the inner boundary heterogeneity.

In contrast, polar vs. equatorial cooling is mostly controlled by inertial effects, as was found by Amit et al. (2020) for homogeneous boundary conditions, with the latitudinally equilibrated inner boundary heterogeneity (Fig. 5 and Table 3) acting to reduce the amplitude of this effect (Fig. 11). Amit et al. (2020) applied their results to Titan's ocean by considering the parametric diagram of Gastine et al. (2016). They found that their models are in the transitional regime between rapidly rotating and non-rotating convection, while Titan's ocean (considering uncertainties in estimated parameters) is either in the same transitional regime or in the non-rotating regime. Because Titan's sub-surface ocean is expected to have stronger inertial effects than our models (see Fig. 10 of Amit et al., 2020), our results seem to suggest that the impact of the heat flux heterogeneity at the bottom of Titan's ocean on the latitudinal cooling pattern at the top of Titan's ocean is secondary. The thinning of Titan's ice shell and corresponding heat flux enhancement in polar regions (Kvorka et al., 2018) can be explained by the polar cooling regime (Amit et al., 2020), and does not require additional heat flux anomalies from the interior.

While the main degree-2 pattern in ice shell thickness and associated heat flux interpreted by Kvorka et al. (2018) can be explained by the oceanic dynamical regime (Amit et al., 2020), the longitudinal variations observed at highest degree (see Fig. 11 of Kvorka et al., 2018) may reflect bottom driven heat flux anomalies. Even though the longitudinal variations are attenuated by ocean dynamics, especially for cases with high Rossby numbers, analysis of these longitudinal fluctuations may provide key constraints on the heat flux coming out of the high-pressure ice mantle, thus constraining its convective dynamics and the efficiency of chemical transfer. However, in order to consistently link the heat flux anomalies to both ocean and high-pressure ice mantle dynamics, a more elaborated description of the ice/ocean interface taking into account melting/freezing processes (see Kvorka et al., 2018, for the upper ocean interface) would ultimately be required. As mentioned above, retroaction between the ocean and ice mantle may impact the heat flux pattern and possibly amplify some specific degrees. Future modeling efforts are needed to take into account a more appropriate boundary condition and its feedback on ocean/ice dynamics. Despite these limitations, the present work provides the first proof of concept on how ocean dynamics may be influenced by bottom heat flux anomalies.

Data availability

Numerical dynamo simulations code: https://magic-sph.github.io/.

Acknowledgments

We thank Guy Moebs for the valuable technical support with the numerical dynamo simulations. Computations were performed on the CCIPL (Le Centre de Calcul Intensif des Pays de la Loire). The source of MagIC (numerical dynamo code) is available at https://magic-sph.github.io/. F. T-N. acknowledges São Paulo Research Foundation (FAPESP), Brazil for grant 2018/07410–3. This study acknowledges the financial support from the French Agence Nationale de Recherche, project ANR COLOSSE (grant N° ANR-2020-CE49-0010).

References

Amit, H., Choblet, G., Olson, P., Monteux, J., Deschamps, F., Langlais, B., Tobie, G., 2015. Towards more realistic core-mantle boundary heat flux patterns: a source of diversity in planetary dynamos. Prog. Earth Planet. Sci. 2, 26. http://dx.doi.org/10.1186/s40645-015-0056-3.

Amit, H., Choblet, G., Tobie, G., Terra-Nova, F., adek, O., Bouffard, M., 2020. Cooling patterns in rotating thin spherical shells – Application to titan's subsurface ocean. Icarus 338, 113509.

Aubert, J., Amit, H., Hulot, G., 2007. Detecting thermal boundary control in surface flows from numerical dynamos. Phys. Earth Planet. Int. 160, 143–156.

Aubert, J., Amit, H., Hulot, G., Olson, P., 2008. Thermo-chemical wind flows couple Earth's inner core growth to mantle heterogeneity. Nature 454, 758–761.

Aubert, J., Brito, D., Nataf, H.-C., Cardin, P., Masson, J.-P., 2001. A systematic experimental study of rapidly rotating spherical convection in water and liquid gallium. Phys. Earth Planet. Int. 128, 51–74.

Aurnou, J., Andreadis, S., Zhu, L., Olson, P., 2003. Experiments on convection in Earth's core tangent cylinder. Earth Planet. Sci. Lett. 212, 119–134.

Aurnou, J., Heimpel, M., Allem, L., King, E., Wicht, J., 2008. Convective heat transfer and the pattern of thermal emission on the gas giants. Geophys. J. Int. 173, 793–801.

Baland, R.-M., Van Hoolst, T., Yseboodt, M., Karatekin, Ö., 2011. Titan's obliquity as evidence of a subsurface ocean? Astron. Astrophys. 530, A141.

Béghin, C., Randriamboarison, O., Hamelin, M., Karkoschka, E., Sotin, C., Whitten, R.C., Berthelier, J.-J., Grard, R., Simões, F., 2012. Analytic theory of Titan's Schumann resonance: Constraints on ionospheric conductivity and buried water ocean. Icarus 218 (2), 1028–1042.

Beuthe, M., 2016. Crustal control of dissipative ocean tides in Enceladus and other icy moons. Icarus 280, 278–299.

Busse, F.H., 1970. Thermal instabilities in rapidly rotating systems. J. Fluid Mech. 44, 441–460.

Čadek, O., Souček, O., Běhounková, M., Choblet, G., Tobie, G., Hron, J., 2019. Long-term stability of Enceladus uneven ice shell. Icarus 310, 476–484.

Čadek, O., Tobie, G., Van Hoolst, T., Massé, M., Choblet, G., Lefèvre, A., Mitri, G., Baland, R.-M., Běhounková, M., Bourgeois, O., et al., 2016. Enceladus's internal ocean and ice shell constrained from Cassini gravity, shape, and libration data. Geophys. Res. Lett. 43, 5653–5660.

Cao, H., Yadav, R.K., Aurnou, J.M., 2018. Geomagnetic polar minima do not arise from steady meridional circulation. Proc. Acad. Nat. Sci. 115, 11186–11191.

Choblet, G., Tobie, G., Sotin, C., Běhounková, M., Čadek, O., Postberg, F., Souček, O., 2017a. Powering prolonged hydrothermal activity inside Enceladus. Nat. Astron. 1 (12), 841.

Choblet, G., Tobie, G., Sotin, C., Kalousova, K., Grasset, O., 2017b. Heat transport in the high-pressure ice mantle of large icy moons. Icarus 285, 252–262.

Choukroun, M., Grasset, O., 2007. Thermodynamic model for water and high-pressure ices up to 2.2 GPa and down to the metastable domain. J. Chem. Phys. 127 (12), 124506.

Choukroun, M., Grasset, O., 2010. Thermodynamic data and modeling of the water and ammonia-water phase diagrams up to 2.2 GPa for planetary geophysics. J. Chem. Phys. 133 (14), 144502.

Deguen, R., Alboussière, T., Cardin, P., 2013. Thermal convection in Earth's inner core with phase change at its boundary. Geophys. J. Int. 194 (3), 1310–1334.

Gastine, T., Wicht, J., Aubert, J., 2016. Scaling regimes in spherical shell rotating convection. J. Fluid Mech. 808, 690–732.

Glatzmaier, G.A., 2002. Geodynamo simulations: how realistic are they? Annu. Rev. Earth Planet. Sci. Lett. 30, 237–257.

Grasset, O., Sotin, C., 1996. The cooling rate of a liquid shell in Titan's interior. Icarus 123 (1), 101–112.

Gubbins, D., Sreenivasan, B., Mound, J., Rost, S., 2011. Melting of the Earth's inner core. Nature 473, 361—363.

Hussmann, H., Sotin, C., Lunine, J.I., 2015. Interiors and evolution of icy satellites. In: Schubert, G. (Ed.), Treatise on Geophysics, second ed. Elsevier, Oxford, pp. 605–635. http://dx.doi.org/10.1016/B978-0-444-53802-4.00178-0.

Iess, L., Jacobson, R.A., Ducci, M., Stevenson, D.J., Lunine, J.I., Armstrong, J.W., Asmar, S.W., Racioppa, P., Rappaport, N.J., Tortora, P., 2012. The tides of Titan. Science 337 (6093), 457–459.

Jara-Orué, H., Vermeersen, B., 2016. Tides on Jupiter's moon Ganymede and their relation to its internal structure. Neth. J. Geosci. - Geol. Mijnb. 95 (2), 191–201.
Kalousová, K., Sotin, C., 2018. Melting in high-pressure ice layers of large ocean worlds–Implications for volatiles transport. Geophys. Res. Lett. 45 (16), 8096–8103.
Kalousová, K., Sotin, C., Choblet, G., Tobie, G., Grasset, O., 2018. Two-phase convection in Ganymede's high-pressure ice layer-implications for its geological evolution. Icarus 299, 133–147.
Khurana, K.K., Kivelson, M.G., Russell, C.T., 2002. Searching for liquid water in Europa by using surface observatories. Astrobiology 2 (1), 93–103.
Khurana, K., Kivelson, M., Stevenson, D., Schubert, G., Russell, C., Walker, R., Polanskey, C., 1998. Induced magnetic fields as evidence for subsurface oceans in Europa and Callisto. Nature 395 (6704), 777–780.
King, E., Buffett, B., 2013. Flow speeds and length scales in geodynamo models: the role of viscosity. Earth Planet. Sci. Lett. 371, 156–162.
King, E., Stellmach, S., Noir, J., Hansen, U., Aurnou, J., 2009. Boundary layer control of rotating convection systems. Nature 447 (7227), 301–304.
Kirk, R., Stevenson, D., 1987. Thermal evolution of a differentiated Ganymede and implications for surface features. Icarus 69 (1), 91–134.
Kivelson, M., Khurana, K., Volwerk, M., 2002. The permanent and inductive magnetic moments of Ganymede. Icarus 157 (2), 507–522.
Kvorka, J., Čadek, O., 2022. A numerical model of convective heat transfer in Titan's subsurface ocean. Icarus 376, 114853.
Kvorka, J., Čadek, O., Tobie, G., Choblet, G., 2018. Does Titan's long-wavelength topography contain information about subsurface ocean dynamics? Icarus 310, 149–164.
Lefevre, A., Tobie, G., Choblet, G., Čadek, O., 2014. Structure and dynamics of titan's outer icy shell constrained from cassini data. Icarus 237, 16–28. http://dx.doi.org/10.1016/j.icarus.2014.04.006.
Long, R.S., Mound, J.E., Davies, C.J., Tobias, S.M., 2020. Scaling behaviour in spherical shell rotating convection with fixed-flux thermal boundary conditions. J. Fluid. Mech. 889, A7.
Lorenz, R., Le Gall, A., 2020. Schumann resonance on titan : Huygens observations critically re-assessed and prospects for the dragonfly mission. In: EGU General Assembly 2020, Online, Vol. EGU2020-2217. pp. 4–8.
Miquel, B., Xie, J., Featherstone, N., Julien, K., Knobloch, E., 2018. Equatorially trapped convection in a rapidly rotating shallow shell. Phys. Rev. Fluids 3 (5), 053801.
Monteux, J., Amit, H., Choblet, G., Langlais, B., Tobie, G., 2015. Giant impacts, heterogeneous mantle heating and a past hemispheric dynamo on mars. Phys. Earth Planet. Int. 240, 114–124.
Mound, J., Davies, C., Rost, S., Aurnou, J., 2019. Regional stratification at the top of Earth's core due to core–mantle boundary heat flux variations. Nat. Geosci. 12, 575–580.
Olson, P., Aurnou, J., 1999. A polar vortex in the Earth's core. Nature 402, 170–173.
Olson, P., Christensen, U.R., 2002. The time averaged magnetic field in numerical dynamos with nonuniform boundary heat flow. Geophys. J. Int. 151, 809–823.
Olson, P., Christensen, U.R., Glatzmaier, G.A., 1999. Numerical modeling of the geodynamo: Mechanisms of field generation and equilibration. J. Geophys. Res. 104, 10383–110404.
Press, W.H., Flannery, B.P., Teukolsky, S., Vetterling, W.T., 1989. Numerical Recipes in FORTRAN: The Art of Scientific Computing. Cambridge University Press, Cambridge, U.K..
Rau, S., Christensen, U.R., Jackson, A., Wicht, J., 2000. Core flow inversion tested with numerical dynamo models. Geophys. J. Int. 141, 485–497.
Saur, J., Duling, S., Roth, L., Jia, X., Strobel, D.F., Feldman, P.D., Christensen, U.R., Retherford, K.D., McGrath, M.A., Musacchio, F., et al., 2015. The search for a subsurface ocean in Ganymede with hubble space telescope observations of its auroral ovals. J. Geophys. Res. 120 (3), 1715–1737.
Soderlund, K.M., 2019. Ocean dynamics of outer solar system satellites. Geophys. Res. Lett. 46 (15), 8700–8710.
Soderlund, K., Schmidt, B., Wicht, J., Blankenship, D., 2014. Ocean-driven heating of Europa's icy shell at low latitudes. Nat. Geosci. 310, 16–19.
Takahashi, F., Tsunakawa, H., Matsushima, M., Mochizuki, N., Honkura, Y., 2008. Effects of thermally heterogeneous structure in the lowermost mantle on the geomagnetic field strength. Earth Planet. Sci. Lett. 272 (3–4), 738–746.
Tobie, G., Gautier, D., Hersant, F., 2012. Titan's bulk composition constrained by Cassini-Huygens: implication for internal outgassing. Astrophys. J. 752 (2), 125.
Tobie, G., Grasset, O., Lunine, J.I., Mocquet, A., Sotin, C., 2005. Titan's internal structure inferred from a coupled thermal-orbital model. Icarus 175, 496–502. http://dx.doi.org/10.1016/j.icarus.2004.12.007.
Tobie, G., Lunine, J.I., Sotin, C., 2006. Episodic outgassing as the origin of atmospheric methane on Titan. Nature 440, 61–64. http://dx.doi.org/10.1038/nature04497.
Vance, S.D., Panning, M.P., Stähler, S., Cammarano, F., Bills, B.G., Tobie, G., Kamata, S., Kedar, S., Sotin, C., Pike, W.T., Lorenz, R., Huang, H.-H., Jackson, J.M., Banerdt, B., 2018. Geophysical investigations of habitability in ice-covered ocean worlds. J. Geophys. Res.: Planets 123 (1), 180–205.
Wicht, J., 2002. Inner-core conductivity in numerical dynamo simulations. Phys. Earth Planet. Int. 132, 281–302.
Willis, P.W., Sreenivasan, B., Gubbins, D., 2007. Thermal core-mantle interaction: Exploring regimes for 'locked' dynamo action. Phys. Earth Planet. Int. 165, 83–92.
Yadav, R.K., Gastine, T., Christensen, U.R., Duarte, L.D.V., Reiners, A., 2016. Effect of shear and magnetic field on the heat-transfer efficiency of convection in rotating spherical shells. Geophys. J. Int. 204, 1120–1133.
Zimmer, C., Khurana, K.K., Kivelson, M.G., 2000. Subsurface oceans on Europa and Callisto: Constraints from Galileo magnetometer observations. Icarus 147 (2), 329–347.